Pergamon

Geochimica et Cosmochimica Acta, Vol. 67, No. 22, pp. 4337–4352, 2003

0016-7037/03 $30.00 + .00

doi:10.1016/S0016-7037(03)00378-8

Quantitative trace element analysis of single fluid inclusions by proton-induced X-ray emission (PIXE): Application to fluid inclusions in hydrothermal quartz

MASANORI KUROSAWA,[1,*] SADAYOSHI SHIMANO,[1] SATOSHI ISHII,[2] KUNIHIRO SHIMA,[2] and TAKUMI KATO[1]

[1]Institute of Geoscience, University of Tsukuba, Tsukuba, Ibaraki 305-8571, Japan
[2]Tandem Accelerator Center, University of Tsukuba, Tsukuba, Ibaraki 305-8577, Japan

(*Received December* 18, 2002; *accepted in revised form April* 23, 2003)

Abstract—Single fluid inclusion analogues with known elemental composition and regular shape were analyzed for trace element contents by particle-induced X-ray emission (PIXE)—a nondestructive method for the analysis of single fluid inclusions—to evaluate the accuracy and detection limits of this type of analysis. Elements with concentrations of 10 to 1000 ppm were measured with average estimated relative error of ±7%. For natural fluid inclusions with 30 μm radius and 20 μm depth in quartz, the total analytical errors were estimated to be ±40% relative for Ca, ±16% for Fe, ±13% for Zn, ±12% for Sr, and ±11% for Br and Rb, by considering uncertainties in microscopic measurements of inclusion depths. Detection limits of 4 to 46 ppm for elements of mass numbers 25–50 were achieved for analyses of a spherical fluid inclusion with 30 μm radius and 20 μm depth in quartz, at an integrated charge of 1.0 μC. The trace element compositions of single fluid inclusions in a hydrothermal quartz crystal were also determined. The elemental concentrations in the inclusions varied widely: 0.2–9 wt.% for Ca and Fe, 300–8000 ppm for Mn and Zn, 40–3000 ppm for Cu, 100–4000 ppm for Br, Rb, Sr, and Pb, and less than 100 ppm for Ge. Elemental concentrations of secondary fluid inclusions on the same trail varied over an order of magnitude, even though all these inclusions were formed from the same fluid. Elemental concentrations in inclusions on the same trail are positively correlated with each other, except for Cu and Rb. Ratios of almost all elements in the inclusions on the trail were essentially unchanged; thus, the elemental ratios can provide original information on trace element compositions of a hydrothermal fluid. *Copyright © 2003 Elsevier Ltd*

1. INTRODUCTION

The elemental composition of fluid inclusions in minerals provides direct information about hydrothermal activities, metasomatism and ore formation processes. Fluid inclusions are commonly small, typically <30 μm; a single mineral grain contains many inclusions of distinctive multiple generations and different compositions. Thus, several techniques for the microanalysis of individual fluid inclusions have been developed to decode changes in fluid activity and geological conditions recorded in single minerals. Synchrotron radiation X-ray fluorescence (SRXRF), laser ablation microprobe-inductively coupled plasma-mass spectrometry (LAM-ICP-MS), and particle induced X-ray emission (PIXE) are the most promising methods for analysis of individual fluid inclusions.

SRXRF is a nondestructive multielement analytical technique based on the measurement of characteristic X-rays generated by an incident X-ray beam of, typically 15 keV potential, from a synchrotron light source. Detection at the low ppm level is possible for mineral analyses. Quantitative trace element analyses of single fluid inclusions have also been reported (Frantz et al., 1988; Vanko et al., 1993; Mosbah et al., 1995; Mavrogenes et al., 1995; Philippot et al., 1998, 2001; Vanko et al., 2001). In SRXRF analysis, the capability of simultaneous multielement analyses can be relatively restricted by the photoelectronic cross section relative to the beam energy. Different beam energies (e.g., 10 and 15 keV) have recently been used for light and heavy element analysis of fluid inclusions (Ménez et al., 2002).

LAM-ICP-MS is a destructive analytical method based on mass spectrometry of small particles ablated from the sample surface by a laser beam (Jackson et al., 1992). Multielement analysis at the low ppb level is possible for solid samples (Horn et al., 1997), and quantification of compositions of single fluid inclusions has been achieved (Rankin et al., 1992; Shepherd and Chenery, 1995; McCandless et al., 1997; Günther et al., 1998; Audétat et al., 1998, 2000a,b; Audétat and Günther, 1999; Ulrich et al., 1999). LAM-ICP-MS is a sensitive technique for analysis of heavy elements of atomic number >57 (La), and useful detection limits are also obtained for light elements (e.g., Li, Be, and B). Since LAM-ICP-MS analysis of unknown fluid inclusion samples usually requires the use of an internal standard (Günther et al., 1998), accurate determination of the concentration of the internal standard by SRXRF or PIXE is necessary for precise analysis.

PIXE is a nondestructive analytical technique based on the measurement of characteristic X-rays induced by a proton microbeam of MeV energy directed onto the specimen surface. Multielement capability, detection at the low ppm level, and full quantitative analysis are all possible with PIXE (Reuter et al., 1975; Maxwell et al., 1989, 1995; Ryan et al., 1990; Czamanske et al., 1993; Campbell, 1995; Kurosawa et al., 1999). Elemental analysis of single fluid inclusions from hydrothermal ore deposits has been demonstrated (Ryan et al., 1991, 1993, 1995; Heinrich et al., 1992; Ballhaus et al., 1994; Damman et al., 1996; Ryan, 1999). Ryan et al. (1993) proposed a reliable basic algorithm for the quantification of fluid inclusions. This algorithm includes three major calculations and

* Author to whom correspondence should be addressed (kurosawa@arsia.geo.tsukuba.ac.jp).

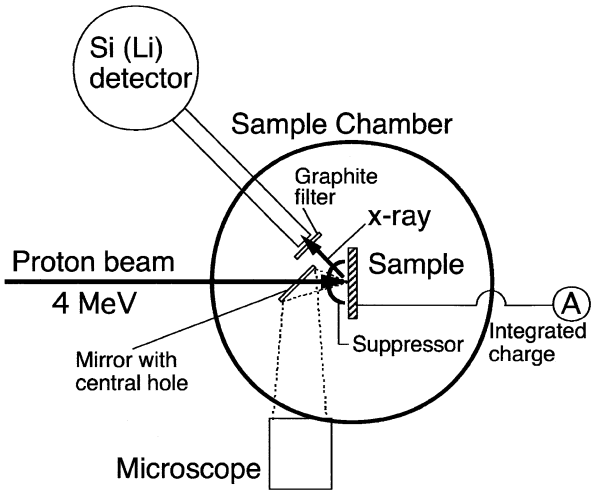

Fig. 1. Schematic diagram of the PIXE instrument. The incident proton beam and the detector angle are at 90° and 135° to a sample surface, respectively. Normal viewing optics with the optical axis collinear to the beam was achieved by using a long-working-distance microscope in conjunction with a mirror with a central hole for beam transmission.

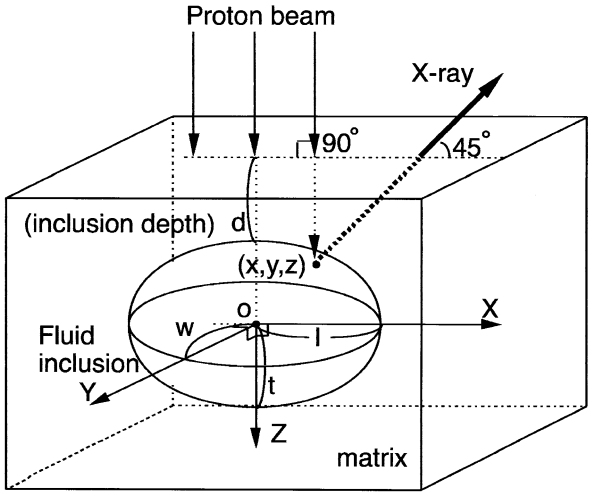

Fig. 2. Schematic geometry for PIXE analysis of fluid inclusions. The distances l, w, and t are the half-length, half-width, and half-thickness of the ellipsoidal fluid inclusion, respectively. The fluid inclusion analog samples are treated as a sphere ($l = w = t$).

corrections necessary for X-ray analysis of inclusions in a sample matrix: energy loss of incident protons in the matrix; intensities of characteristic X-rays emitted from the whole inclusion; and absorption of the X-rays by the matrix. PIXE is currently the most precise X-ray analytical method for analysis of single fluid inclusions. The analytical error for major elements in synthetic single fluid inclusions has been estimated at ±15% relative (Ryan et al., 1995), and the total analytical error for natural fluid inclusion measurements at ±30% relative (Ryan, 1999). However, errors on trace element data have not been evaluated.

Here, we use PIXE to determine the trace element composition of single fluid inclusion analogues with known chemical compositions and regular shapes. We have evaluated the accuracy and detection limits of the analytical method. In addition, we have determined the trace element composition of single fluid inclusions from a hydrothermal quartz crystal to examine compositions of a hydrothermal fluid derived from a granitic system.

2. EXPERIMENTAL METHODS

2.1. The PIXE Instrument

Fluid inclusion samples were analyzed at the PIXE facility at the Tandem Accelerator Center, University of Tsukuba. A 4-MeV proton beam was focused using slits and magnetic lenses on a ca. 50 × 100 to 300 × 300 μm^2 spot on the sample surface. Beam incidence was normal to the sample surface, and the X-ray measurement take-off

Table 1. Fluid inclusion analogue samples and proton beam conditions for the PIXE measurements.

Run no.	Content[a] (ppm)	Inclusion radius (μm)	Degree[b] of filling (%)	Cover glass thickness (μm)	Beam current (nA)	Integrated charge (μC)
Aug23Q4	1000	50	70	10	0.3	1.0
Aug23S1	1000	75	50	10	0.3	1.0
Oct17G1	1000	75	85	20	0.3	0.5
Oct17G2	1000	105	64	20	0.3	0.5
Oct17F2	500	125	89	20	0.3	0.5
Jan10G1	500	120	100	10	0.3	0.5
Jan10E0	500	105	100	10	0.3	0.5
Oct17H1	100	60	94	20	0.3	0.75
Oct17H3	100	48	86	20	0.3	0.75
Jan10F2	100	140	100	10	0.2	1.0
Oct18D123	50	75	94	20	0.3	1.5
Jan11C0	50	100	100	10	0.2	1.5
Jan11B0	50	105	100	10	0.2	2.5
Nov28C1	10	100	100	10	0.4	3.0
Nov28C2	10	100	100	10	0.4	3.0

[a] Concentration of multielement standard solution in fluid inclusion analogue samples. The solution contains Cr, Ni, Fe, Zn, Ga, Ge, Sr, Mo, Ag, Cd, In, and Ba.
[b] Degree of filling of the standard solution in the fluid inclusion analogue samples.

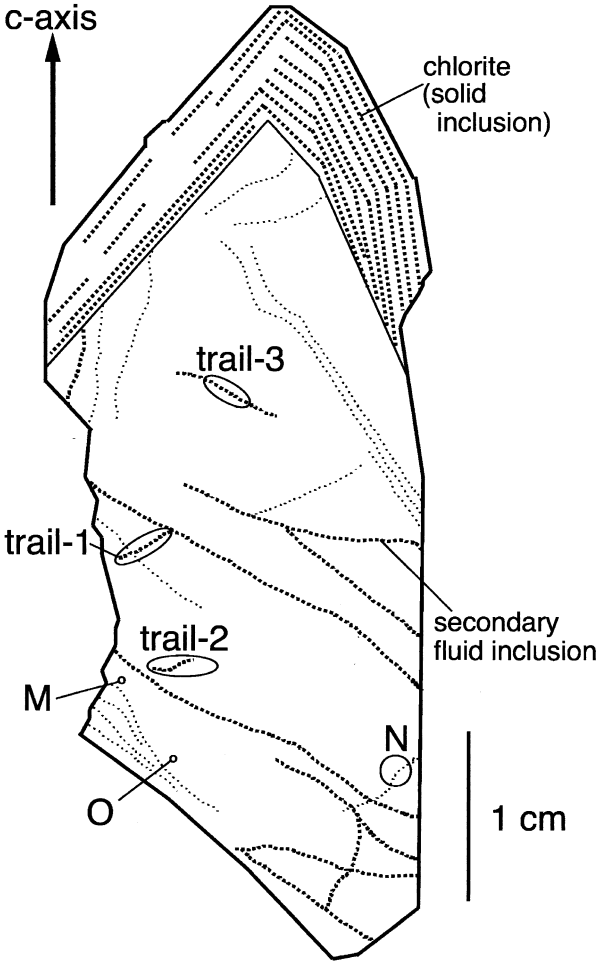

Fig. 3. Schematic cross section of a euhedral quartz crystal from the Kawahage quartz veins at Kawakami village, Nagano Prefecture, in central Japan. The sample (200-μm thick, 5-cm long) was cut parallel to the c-axis and contained tiny chlorite crystals as solid inclusions along the top rim. Analyzed fluid inclusions were selected from three trails of secondary fluid inclusions (trail 1, trail 2, and trail 3), a pair of fluid inclusions formed during the necking-down process (N-1 and N-2), and large, isolated fluid inclusions (M and O). Almost all inclusions were ellipsoidal (30 μm in size) and contained saline water, vapor bubbles, and halite crystals (Table 2).

angle was 45° (Fig. 1). The beam spot and analytical points were observed with an optical viewing system using a charge-coupled device camera mounted on a microscope (Kurosawa et al., 1998). The beam diameter, determined from the beam radiation-induced fluorescence from fluorescent materials, was set to be larger than the diameter of the fluid inclusion samples. The irradiated area corresponded to the central part of the beam, so the flux density of the beam in the sampled area was assumed to be uniform.

The chamber pressure was maintained below 10^{-4} Pa to avoid defocusing of the beam due to scattering by residual gas. The characteristic X-rays excited by the incident beam were detected by a Si(Li) X-ray energy detector with a nominal resolution of 145 eV at 5.9 keV, and the spectra were recorded by a multichannel analyzer. A 1.3-mm-thick graphite filter was located between the specimen and the detector to attenuate the intense X-rays from the predominant light elements and to prevent the entry into the detector of 4-MeV protons scattered from samples (Fig. 1). The beam current was set at 0.3–1.5 nA to obtain good counting statistics and minimize sample damage. The total charge was determined by integrating the target currents, and all samples were analyzed to integrated charges of 0.5 to 5.0 μC. A suppressor electrode was placed near the sample surface to prevent loss of integrated charge by secondary electron emission from insulating matrices such as SiO_2 (Fig. 1).

2.2. PIXE Quantification

Quantification was performed based on the model of Ryan et al. (1993). In this model, the element of interest is situated at a discrete point (x,y,z) within a fluid inclusion buried in a sample matrix. The intensities of the generated X-rays are calculated by considering the attenuation of energy of the incident protons and the absorption of the X-rays by the matrix and the fluid (Fig. 2).

Integrating the X-ray intensity over the entire volume of the fluid inclusion provides the total X-ray intensity. Theoretical X-ray intensities for each element/1 ppm of a model fluid inclusion are first calculated by volume integration using physical parameters of the sample materials, the measurement geometry and conditions, and size of the model inclusion. The model inclusion, which is assumed to exist in the same matrix as the real sample, is set as an ellipsoidal equal to the size and inclusion depth of the measured fluid inclusion. The fluid inclusion analog is treated as a sphere ($l = w = t$). The required parameters for the theoretical calculations are the major element composition, the densities of the matrix and the fluid, their proton-stopping powers, the X-ray production cross sections, the X-ray absorption coefficients, and the detector sensitivity for each element.

The required parameters were known for the fluid inclusion analog samples. For natural fluid inclusion samples, the fluid was approximated as H_2O and the density was corrected with reference to estimates of the salinity and the degree of filling. The inclusion sizes and depths were determined with an optical microscope.

In the theoretical calculations, Ryan's (1993) method also corrects for contributions of X-rays from impurities in the matrix and bubbles in the fluid inclusion. The measured X-ray intensities for each element of interest in the inclusion are divided by the theoretical X-ray intensities/1 ppm and converted to element concentrations. Details of the quantification method are presented in Appendix 1.

2.3. Determination of Inclusion Depth of a Natural Fluid Inclusion

The inclusion depth, length, width, and thickness of a natural sample (Fig. 2) were determined by using the fine focus knob of an optical microscope with a 40× objective. The thickness of the inclusion was estimated from the length and width on the basis of the orientation and regular negative-crystal shape of most natural inclusions. Inclusion depth was determined by measuring the distance between the sample surface and the waist of the inclusion, which was sharply outlined. This determination is more reproducible than distance measurements between the surface and the top of the inclusion (Heinrich et al., 1992). The measured distances were affected by the refractive index of the matrix, so an appropriate correction was applied. The inclusion depth was calculated by subtracting half of the estimated inclusion thickness from the corrected distance.

3. SAMPLES

3.1. Fluid Inclusion Analog Samples with Known Concentration and Shape

Fluid inclusion analog samples were prepared by filling air bubble pockets on the surface of a 1-mm-thick fused-quartz glass plate with a multielement standard solution. The samples, 50 to 140 μm in radius, were covered with 10- or 20-μm-thick fused-quartz glass films. The diameter of the truncation, the aperture size of the bubble pockets, is about half of the bubble's diameter. The corresponding volumes are small compared to whole volumes of bubble pockets. The thickness of the glass films was measured with a digital micrometer (resolution: 1 μm) and an interferometer (practical resolution: 0.03 μm). The

Table 2. Fluid inclusion samples in a quartz crystal from Kawahage and analytical conditions applied.

Sample	Type[a]	Feature	Halite dissolution temp. (C°)	Homogenization temp. (C°)	Salinity[b] (wt.%)	Inclusion size[c] l × w × t (μm × μm × μm)	Bubble radius (μm)	Inclusion depth (μm)	Beam current (nA)	Integrated charge (μC)
G-1	trail-1	halite + bubble	184.1	406.5	30.4	15.0 × 15.0 × 15.0	7.5	31.5	0.35	2.0
G-2	trail-1	halite + bubble	165.0	389.0	30.3	20.0 × 10.0 × 10.0	5.5	33.4	0.35	2.0
G-3	trail-1	halite + bubble	165.0	389.1	30.3	15.0 × 12.5 × 12.5	6.0	32.5	0.35	2.0
G-1	trail-1	halite + bubble	165.0	401.2	30.3	11.0 × 9.0 × 11.0	5.0	7.6	0.08	0.5
G-2	trail-1	halite + bubble	166.6	389.1	29.9	10.0 × 6.0 × 6.0	4.0	25.0	0.08	0.5
F-4	trail-1	halite + bubble	153.2	396.8	30.1	20.0 × 10.0 × 10.0	6.0	21.0	0.35	1.5
F-3	trail-1	halite + bubble	161.2	388.1	30.3	15.0 × 9.0 × 9.0	5.0	23.5	0.35	1.5
F-2	trail-1	halite + bubble	166.8	405.3	29.4	15.0 × 10.0 × 10.0	5.0	21.0	0.35	1.5
F-1	trail-1	halite + bubble	141.1	272.3	30.2	15.0 × 11.0 × 11.0	5.5	20.0	0.35	1.5
H-1	trail-1	halite + bubble	166.8	403.1	30.5	11.0 × 9.0 × 9.0	6.0	6.5	0.50	0.5
H-2	trail-1	halite + bubble	170.3	404.0	27.1	12.5 × 12.5 × 12.5	5.0	10.8	0.50	0.5
J-1	trail-2	halite + bubble	248.9	329.0	34.6	30.0 × 10.0 × 10.0	6.0	28.8	0.08	0.5
J-2	trail-2	halite + bubble	249.0	283.6	34.3	11.0 × 11.0 × 11.0	5.0	9.2	0.08	0.5
J-3	trail-2	halite + bubble	243.1	318.7	33.9	14.0 × 9.0 × 9.0	6.0	58.9	0.08	0.5
J-4	trail-2	halite + bubble	237.0	308.0	27.4	40.0 × 10.0 × 10.0	5.0	21.0	0.08	0.5
K-1	trail-3	bubble	—	360.3	—	20.0 × 20.0 × 20.0	12.5	18.8	0.08	0.5
K-2	trail-3	bubble	—	359.0	—	22.5 × 17.5 × 20.0	15.0	22.8	0.08	0.5
K-3	trail-3	bubble	—	359.6	—	25.0 × 20.0 × 20.0	12.5	34.3	0.08	0.5
K-4	trail-3	bubble	—	357.8	—	20.0 × 15.0 × 15.0	14.0	23.8	0.08	0.5
M-1	huge, isolated	halite + bubble	239.0	350.6	27.4	50.0 × 20.0 × 20.0	12.5	11.0	0.05	0.5
O-1	huge, isolated	halite + bubble	296.0	326.4	27.7	45.0 × 20.0 × 20.0	10.0	11.0	0.05	0.5
N-1	necking-down	halite, no bubble	150.0	256.0	27.0	15.0 × 15.0 × 10.0	0.0	5.5	0.05	0.5
N-2	necking-down	bubble, no halite	—	200.0	—	20.0 × 10.0 × 10.0	5.0	27.2	0.05	0.3

[a] Three trails of secondary fluid inclusions: isolated fluid inclusions; pair of fluid inclusions formed during necking-down process.
[b] Calculated after Sterner et al. (1988).
[c] l, w, and t are the half-length, half-width, and half-thickness of the fluid inclusions.

cover glass was fixed with a resin to prevent loss of the solution during irradiation in the vacuum chamber. The multielement standard solutions were XSTC-531, -532, -533, -534, and -535 (SPEX Co. Ltd., Metuchen, New Jersey) that contained 10, 50, 100, 500, and 1000 ppm of Cr, Ni, Fe, Zn, Ga, Ge, Sr, Mo, Ag, Cd, In, and Ba in 5% nitric acid solution, respectively (Table 1). Several samples contained small air bubbles, so microscopic observation was used to determine the actual liquid volume and correct for the presence of air bubbles (see Appendix 1). No impurities with concentrations greater than 1 ppm in the glass plates and glass films were detected by LAM-ICP-MS. The density of the glass plates and glass films was 2.23 g/cm^3. The samples were coated with a carbon film to prevent electrostatic charging and to measure the integrated charges. At a beam current of less than 0.4 nA, no fluid leaked from the samples during irradiation in the vacuum chamber.

3.2. Fluid Inclusion Samples in Hydrothermal Quartz

The quartz sample for the analysis of natural fluid inclusions was collected from quartz veins at Kawahage, Kawakami village, Nagano Prefecture, in central Japan. The quartz veins intrude Mesozoic sandstone, mudstone, and limestone strata and are genetically related to a Miocene biotite granite body at 800 m distance from the veins. Fe-Cu mines of the skarn type, considered to have the same hydrothermal origin, are present near the veins. The veins are of a simple hydrothermal quartz type that laterally grades into skarn bodies. The main quartz part has a large amount of single quartz crystals and a small amount of chlorite; the skarn part contains calcite, quartz, hedenbergite, vesuvianite, andradite, and scapolite.

The quartz sample for this experiment was a euhedral crystal, 5 cm in length, from a druse in the main quartz part of a vein, and contained tiny chlorite crystals as solid inclusions in its tip (Fig. 3). A 200-μm-thick slice was cut from the sample parallel to the c-axis, mounted on a glass slide, and polished. Cross-polarized light revealed Brazil twinning only at the rim of the tip of the crystal. No fibrous growth or deformation lamellae were observed in the crystal.

Large, isolated, primary fluid inclusions, three trails of secondary fluid inclusions, and a pair of fluid inclusions formed during the necking-down process were selected for measurement (Table 2). All inclusions analyzed contained saline water, vapor bubbles, and halite crystals (Fig. 4a), except for fluid inclusions on trail 3. The large isolated inclusions (100 μm in length) were of irregular shapes. Trail 1 consisted of more than 30 secondary inclusions arranged over 3 mm in the quartz specimen (Fig. 3). The 11 inclusions measured had a negative-crystal shape and ellipsoidal (major axis 10–30 μm) shapes (Fig. 4b and Table 2). Trail 2 consisted of approximately 30 secondary inclusions arranged over 2 mm in the quartz specimen. The four inclusion samples measured were irregularly shaped (20–60 μm in size) (Table 2). Trail 3 consisted of approximately 30 secondary inclusions arranged over 3 mm in the quartz specimen. The four inclusion samples measured had a negative crystal shape (30–50 μm in size) (Table 2). The pair of fluid inclusions was divided into two inclusions. One inclusion contained a halite crystal and no bubble, and the other inclusion contained a bubble and no halite crystal, respectively (Fig. 4c,d); both were flat (30–40 μm in size), and a small conduit connecting these inclusions was observed.

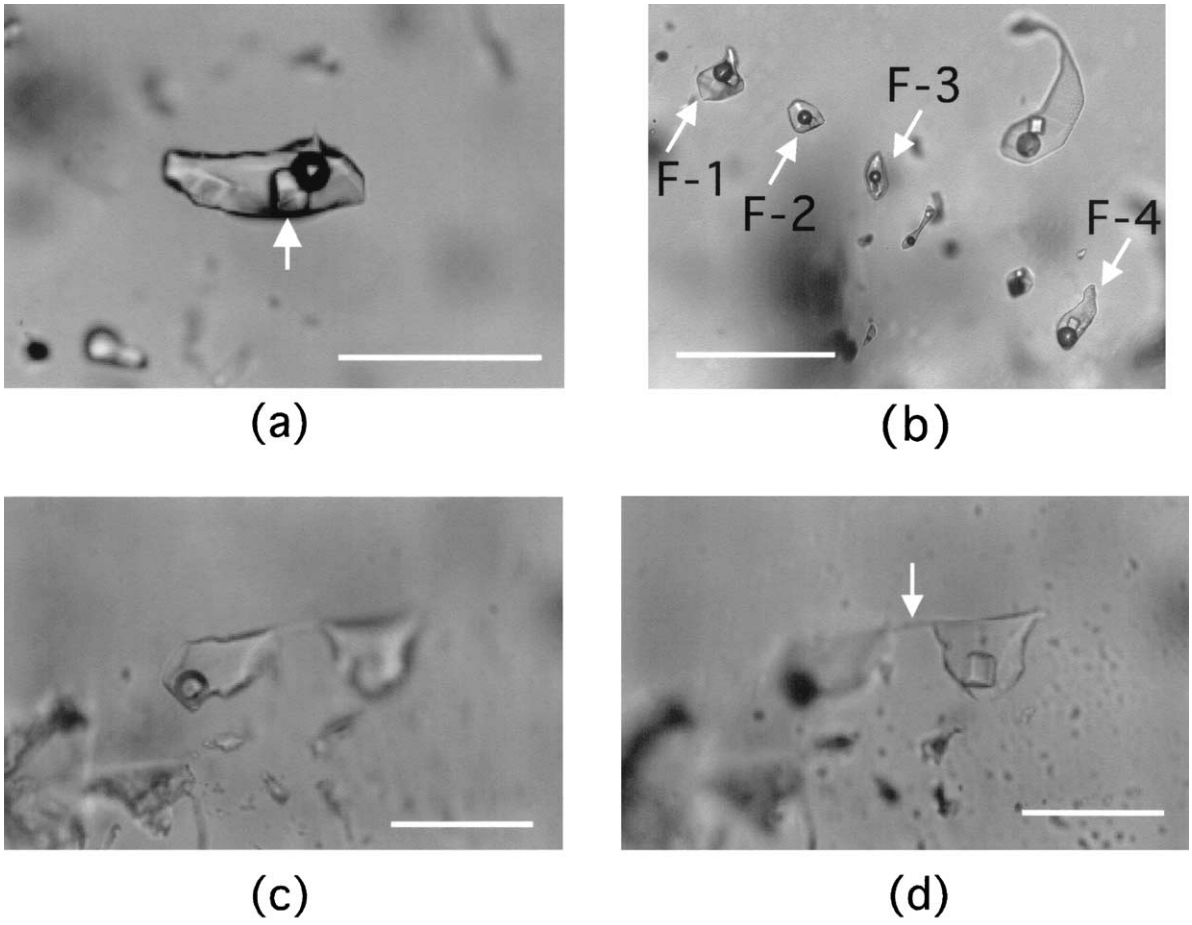

Fig. 4. (a) Isolated large brine inclusion with halite crystal (white arrow) (sample O). Scale bar is 100 μm. (b) Fluid inclusions of trail 1 (sample F). White arrows represent inclusion samples F-1, F-2, F-3, and F-4. Scale bar is 100 μm. (c) One of the paired brine inclusions formed during the necking-down process. The inclusion, designated N-2, contains a bubble but no halite crystal. Scale bar is 50 μm. (d) The second of the paired brine inclusions formed during the necking-down process. The inclusion, designated N-1, contains a halite crystal but no bubble. A small conduit connecting inclusions N-1 and N-2 is shown (white arrow). Scale bar is 50 μm.

4. RESULTS

4.1. Determination of Trace Elements in Fluid Inclusion Analog Samples and Accuracy of the PIXE Analyses

Measured spectra of the fluid inclusion analog samples consisted of the Kα and Kβ peaks from Cr, Fe, Ni, Zn, Ga, Ge, Sr, Mo, Ag, Cd, In, and Ba (Fig. 5a–c). Except for Ba, all of these elements could still be detected at a concentration of 10 ppm (corresponding to 4.2×10^{-11} g as solute) (Fig. 5c). Ba could not be detected at this concentration because of the relatively low sensitivity of the Si(Li) detector in the high-energy X-ray region (Appendix 2).

The concentrations determined for almost all of the elements in these samples agreed with the original concentrations within $\pm$10% relative difference (Table 3). At low concentrations, In and Ba in some samples were not detected because of the relatively low sensitivity of the detector to these elements. At concentrations less than 100 ppm, analytical results for Sr and Mo in samples Jan11B0, Nov28C1, and Nov28C2 exhibited large relative differences (Table 3). These large differences are attributed to a strong selective adsorption of Sr and Mo onto the adhesive resin used to fix the cover glass. X-rays from the selectively absorbed Sr and Mo did not pass through the matrix and solution before reaching the detector. Consequently, these X-rays had a shorter path length and were more intense than X-rays from Sr and Mo in the samples. Selective adsorption of Sr and Mo was confirmed by PIXE measurements of materials where the adhesive was in contact with the standard solution. Molybdenum in Aug23S1, at a concentration of 1000 ppm, also showed a large relative difference; however, the reason for this is not evident.

Calculated and original values for the samples are compared in Figure 6 and Table 4. Calculated values are mean values of several analyses for each concentration, except for the above-mentioned Sr and Mo data with large relative differences. The error bars in Figure 6 represent 1σ standard deviations. Calculated values agreed with the original values over the concentration range of 10 to 1000 ppm within the observed precision, showing the validity of the present quantification for trace elements in fluid inclusions. The average accuracy of these

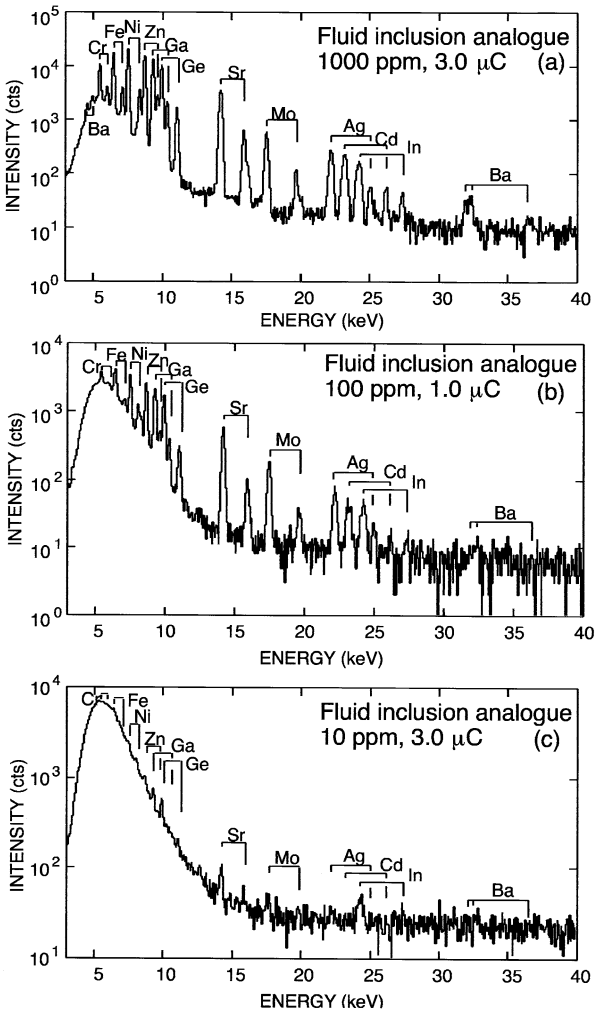

Fig. 5. X-ray spectra of fluid inclusion analogues containing multielement standard solutions with concentrations of 1000 $\mu g\ g^{-1}$ (a), 100 $\mu g\ g^{-1}$ (b), and 10 $\mu g\ g^{-1}$ (c). The standard solutions contained Cr, Fe, Ni, Zn, Ga, Ge, Sr, Mo, Ag, Cd, In, and Ba. Radii of the inclusion analogues are 75, 140, and 100 μm for (a), (b), and (c), respectively. The spectra were measured by PIXE (4-MeV protons, 1.3-mm-thick graphite filter, integrated charges of 3.0 μC [spectra a and c] and 1.0 μC [spectrum b]).

determinations was $\pm$7% mean relative difference over the concentration range.

Detection limits for trace elements in a spherical fluid inclusion with 30 μm radius and 20 μm depth in quartz were determined (Fig. 7, Table 5). The detection limits at 99% confidence level were calculated from 3 times the statistical error for the computed backgrounds and the overlapping peak intensities at an integrated charge of 1.0 μC. Typical detection limits were in the range of 4 to 46 ppm for elements of mass number 25–50 (Table 5).

4.2. Uncertainty of Microscopic Determination of Inclusion Depth and Total Analytical Error

Accurate determination of the inclusion depth is important for the quantification of trace elements in fluid inclusions, because inclusion depths influence calculations of X-ray absorption by matrix and fluid. As we determined inclusion depths by microscopic measurements, errors due to adjustment of the fine focus knob of the microscope and aberration of the optics could occur. Thus, we also estimated the error on the microscopic measurements by measuring the depths of several bubbles buried in a quartz glass.

The quartz glass was a rectangular column of $5 \times 5 \times 10$ mm^3 geometry, and contained many bubbles of 20–55-μm diameter. The distance between the glass surface and the waist of a bubble in the glass was determined by microscopic measurements from the surface (Fig. 7a). The measured distance (D_{meas}) was affected by refraction by the matrix and by errors related to the microscopic measurements. Thus, the errors can be estimated by comparing the measured distance corrected for refraction and the actual distance (D_{actual}) (Fig. 7a). Because the measured bubbles leaned to the front side, D_{actual} was easily determined by measurements from the front face without effects of refraction and errors due to microscopic measurements (Fig. 7a).

The distance calculated based on D_{meas} and the refractive index ($n = 1.46$) agreed well with the actual distance (Fig. 7b). The mean difference was $\pm$2.6 μm for bubbles with an actual depth of 30–100 μm. The error for repeated measurements of single bubbles was of the order of $\pm$2 μm, which is smaller than the error of the mean difference. Thus, the uncertainty for the microscopic determination of the inclusion depth was estimated to be $\pm$2.6 μm over the range of depth from 30 to 100 μm.

Relative errors due to $\pm$2.6-μm depth uncertainty for a spherical fluid inclusion with 30-μm radius and 20-μm deep in quartz are listed in Table 5. The relative error depended on the X-ray energy for each element. Taking into account uncertainties in the inclusion depth measurements and the quantification of this parameter, we estimated the total analytical error for quantitative PIXE analyses of fluid inclusions in quartz to be $\pm$40% relative for Ca, $\pm$16% for Fe, $\pm$13% for Zn, $\pm$12% for Sr, and $\pm$12% for Br and Rb (Table 5).

4.3. Trace Element Contents of Fluid Inclusions in Hydrothermal Quartz

The spectrum of the large isolated fluid inclusion (sample O) consisted of the K X-ray peaks from Ca, Mn, Fe, Cu, Zn, Br, Rb, and Sr, and of the L X-ray peaks from Pb (Fig. 8a). L X-ray peaks from Ba, La, and Ce, and K X-ray peak from Ni were also visible (Fig. 8a), although these elements could not be determined because of the low intensities. The other isolated inclusion (sample M) gave a similar spectrum. In the all-quartz matrix, a small Cu peak, corresponding to a Cu concentration of 4 ppm, was observed (Fig. 8b). Hydrothermal quartz crystals sometimes contain 0–7 ppm Cu, normally less than 4 ppm (Weise et al., 1993; Götze et al., 2001), and Cu^{+} or Cu^{2+} are thought to be incorporated into quartz crystals together with alkali ions to compensate a charge deficiency due to the presence of trivalent cations in the lattice (Weil, 1984). Thus, a correction for Cu X-rays from the matrix was performed for the quantification of Cu in all natural fluid inclusions (Appendix 1).

Secondary fluid inclusions of trails 1 and 2 gave spectra that were similar to the spectra of the isolated inclusions. Ba, La, Ce, and Ni were not detected. Ca was observed only in trail 2 because of the higher detection limit of Ca. Fluid inclusions on

Table 3. Analytical PIXE results for fluid inclusion analogue samples.

	Aug23Q4 (1000 ppm)[a]			Aug23S1 (1000 ppm)			Oct17G1 (1000 ppm)			Oct17G2 (1000 ppm)			Oct17F2 (500 ppm)		
	Int. (cts)[b]	Conc. (ppm)	Err. (%)	Int. (cts)	Conc. (ppm)	Err. (%)	Int. (cts)	Conc. (ppm)	Err. (%)	Int. (cts)	Conc. (ppm)	Err. (%)	Int. (cts)	Conc. (ppm)	Err. (%)
Cr	21960	1004	(0)	38249	1081	(8)	2195	1086	(9)	3210	925	(8)	2407	545	(9)
Fe	37356	1001	(0)	64575	1018	(2)	5363	953	(5)	9569	979	(2)	6821	550	(10)
Ni	43507	1038	(4)	78736	1069	(7)	8801	979	(2)	14433	920	(8)	9756	491	(2)
Zn	34202	939	(6)	66040	1012	(1)	9128	945	(6)	14973	888	(11)	10649	501	(0)
Ga	30698	950	(5)	53749	923	(8)	10349	1152	(15)	14229	910	(9)	9772	496	(1)
Ge	27407	827	(17)	49127	819	(18)	9191	1154	(15)	13187	952	(5)	8917	511	(2)
Sr	7709	910	(9)	18043	1175	(18)	2641	1151	(15)	4453	1131	(13)	2912	591	(18)
Mo	3326	918	(8)	3447	530	(47)	864	986	(1)	1573	1057	(6)	1047	563	(13)
Ag	666	991	(1)	1153	968	(3)	248	896	(10)	347	746	(25)	222	382	(24)
Cd	554	1028	(3)	1040	1090	(9)	227	1046	(5)	347	952	(5)	238	524	(5)
In	458	1058	(6)	736	964	(4)	167	984	(2)	235	824	(18)	169	476	(5)
Ba	50	1098	(10)	76	967	(3)	19	1003	(0)	32	1029	(3)	17	445	(11)

	Jan10G1 (500 ppm)			Jan10E0 (500 ppm)			Oct17H1 (100 ppm)			Oct17H3 (100 ppm)			Jan10F2 (100 ppm)		
	Int. (cts)	Conc. (ppm)	Err. (%)	Int. (cts)	Conc. (ppm)	Err. (%)	Int. (cts)	Conc. (ppm)	Err. (%)	Int. (cts)	Conc. (ppm)	Err. (%)	Int. (cts)	Conc. (ppm)	Err. (%)
Cr	6789	554	(11)	5174	462	(8)	189	111	(11)	116	108	(8)	4352	108	(8)
Fe	13988	518	(4)	11099	450	(10)	540	117	(17)	274	96	(4)	8594	97	(3)
Ni	15386	457	(9)	17773	577	(15)	689	94	(6)	406	92	(8)	10715	97	(3)
Zn	14185	483	(3)	13504	501	(0)	770	99	(1)	334	72	(28)	9234	96	(4)
Ga	10748	428	(14)	12373	537	(7)	663	92	(8)	385	90	(10)	8094	99	(1)
Ge	8884	428	(14)	10348	542	(8)	692	108	(8)	320	84	(16)	6979	103	(3)
Sr	2802	564	(13)	1888	411	(18)	177	96	(4)	83	75	(25)	2520	157	(57)
Mo	913	484	(3)	891	510	(2)	62	87	(13)	46	108	(8)	752	123	(23)
Ag	323	531	(6)	245	434	(13)	19	83	(17)	11	81	(19)	203	104	(4)
Cd	250	522	(4)	264	593	(19)	15	85	(15)	10	94	(6)	154	100	(0)
In	210	555	(11)	190	542	(8)	18	128	(28)	—	—	—	112	92	(8)
Ba	21	476	(5)	9	216	(57)	—	—	—	—	—	—	12	85	(15)

	Oct18D123 (50 ppm)			Jan11C0 (50 ppm)			Jan11B0 (50 ppm)			Nov28C1 (10 ppm)			Nov28C2 (10 ppm)		
	Int. (cts)	Conc. (ppm)	Err. (%)	Int. (cts)	Conc. (ppm)	Err. (%)	Int. (cts)	Conc. (ppm)	Err. (%)	Int. (cts)	Conc. (ppm)	Err. (%)	Int. (cts)	Conc. (ppm)	Err. (%)
Cr	273	53	(5)	1812	53	(6)	2666	52	(3)	242	9	(10)	239	11	(8)
Fe	768	53	(6)	3403	45	(10)	5246	46	(8)	455	10	(2)	422	9	(9)
Ni	1074	46	(7)	5067	54	(8)	6105	43	(14)	599	10	(4)	479	8	(17)
Zn	1033	42	(17)	3831	46	(7)	6126	49	(1)	462	9	(11)	420	8	(19)
Ga	1035	45	(10)	3835	54	(9)	5078	48	(5)	521	11	(14)	515	11	(13)
Ge	1058	52	(3)	3271	56	(12)	4287	49	(3)	525	13	(34)	579	15	(48)
Sr	296	50	(0)	710	50	(1)	1946	92	(84)	252	22	(116)	246	21	(111)
Mo	95	42	(16)	304	57	(13)	671	83	(66)	103	21	(114)	41	9	(15)
Ag	41	58	(16)	88	51	(1)	104	40	(20)	15	10	(3)	13	8	(15)
Cd	32	57	(15)	70	51	(2)	115	56	(12)	10	8	(16)	10	8	(18)
In	25	56	(13)	50	46	(7)	78	48	(4)	13	14	(42)	8	9	(8)
Ba	2	41	(19)	7	55	(9)	8	40	(19)	—	—	—	—	—	—

— = undetected; Conc. = determined concentrations; Err. = relative error, original value − determined value ÷ (original value).
[a] Original concentrations of multielement standard solution in fluid inclusion analogue samples.
[b] Int. (cts) = measured X-ray intensities (counts).

trail 3 showed peaks of only Cu, Ge, and Pb. The very different spectra reflect the various fluids trapped in a single quartz crystal.

The elemental concentrations determined in the natural inclusion samples are listed in Table 6. In general, the concentrations varied widely for each inclusion: 0.2–9 wt.% for Ca and Fe, 300–8000 ppm for Mn and Zn, 40–3000 ppm for Cu, 100–4000 ppm for Br, Rb, Sr, and Pb, and less than 100 ppm for Ge. Elemental concentrations differed by an order of magnitude in inclusions on the same fluid inclusion trail (trail 1) (Fig. 9). No clear relationship between spatial distribution in the quartz and elemental content in inclusions is observed for each of these trails.

5. DISCUSSION

5.1. Uncertainty on Natural Fluid Inclusion Analysis by PIXE

In the present quantification for natural fluid inclusions, other possible error sources are three approximations for fluid, a

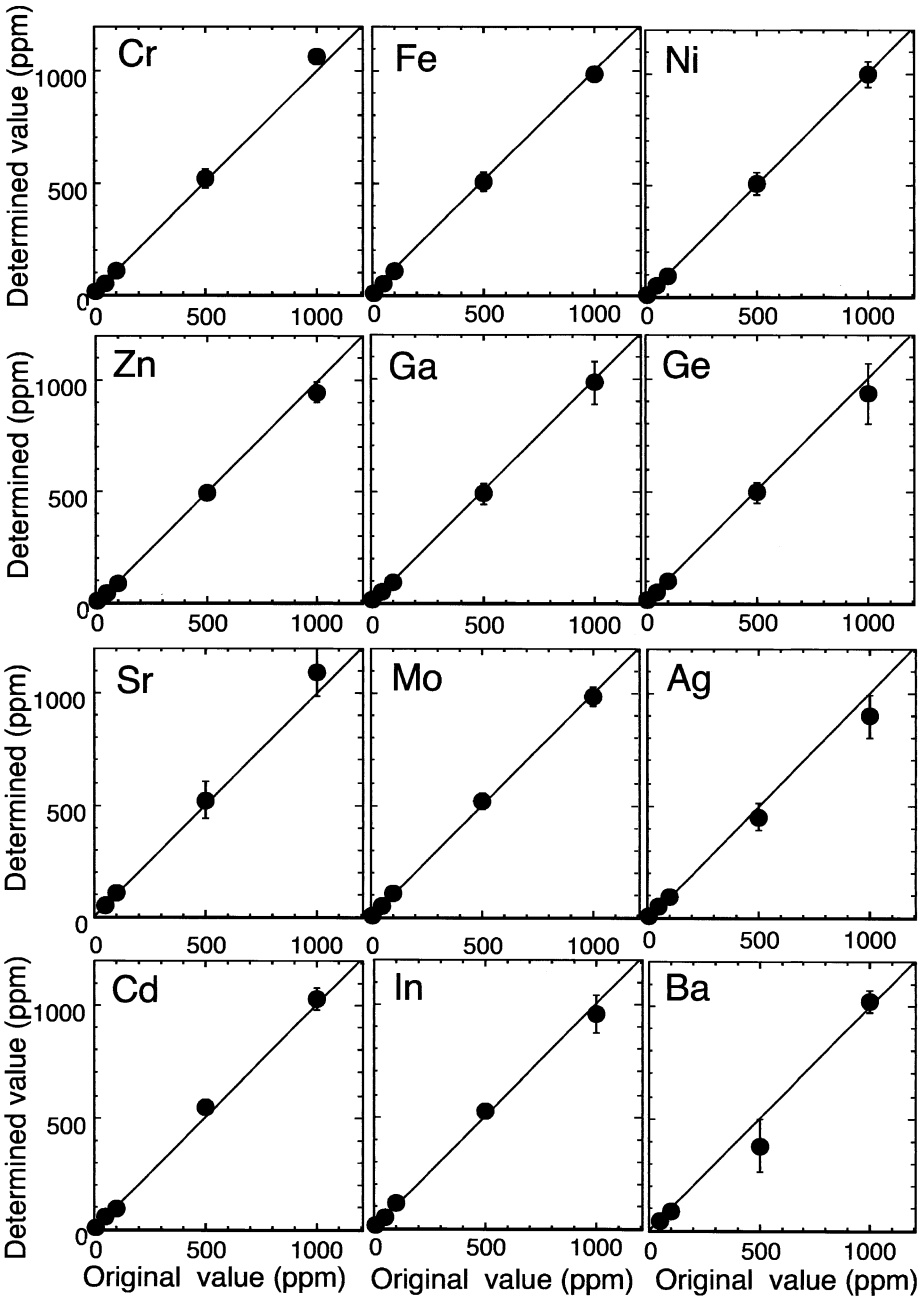

Fig. 6. Comparison of measured and original elemental concentrations in fluid inclusion analog samples. The measured values are mean values of several PIXE analyses for each concentration, and the error bars represent 1σ standard deviations (Table 4). All data fell onto a straight line of slope 1, within the experimental precision.

presence of halite daughter crystals, and inclusion shapes. Fluid in natural samples was approximated as H_2O, and the density was only corrected with reference to estimates of the salinity (30% NaCl) and the degree of filling (Appendix 1). By assuming fluid as pure water with a corrected density of 1.10 g/cm^3, elemental concentrations in spherical fluid inclusions with 30 μm diameter, 10 μm inclusion depth, volume ratio 0.8, and salinity of 30% NaCl are estimated at several % higher or lower values than the true concentrations. The over- and underestimation is calculated at +7% relative, +5%, +1%, +1%, −3%, and −1% for Mn, Fe, Cu, Zn, Sr, and Pb, respectively. These values are smaller than the above-mentioned total analytical error, thus the effect for the present natural inclusion analyses is considered small.

For the effect of halite crystals, a portion of halite in a fluid inclusion is more important than an effect of secondary fluorescence X-rays from the halite, because natural halite crystals contain almost no heavy transition metal elements. The present quartz sample with inclusions was fixed perpendicular to the horizontal proton beam in the sample chamber, so that a portion of a small halite crystal in ellipsoidal fluid inclusions should

Table 4. Summary of quantitative PIXE data for fluid inclusion analogue samples.

	1000 ppm content[a]			500 ppm content			100 ppm content			50 ppm content			10 ppm content		
	value[b] (ppm)	SD (1σ)	err. (%)	value (ppm)	SD (1σ)	err. (%)	value (ppm)	SD (1σ)	err. (%)	value (ppm)	SD (1σ)	err. (%)	value (ppm)	SD (1σ)	err. (%)
Cr	1063	(34)	6	521	(42)	4	109	(1)	8	52	(1)	4	11	—	8
Fe	988	(24)	1	506	(42)	1	103	(9)	3	48	(4)	4	9	(1)	6
Ni	1001	(57)	0	509	(50)	2	95	(2)	6	48	(5)	5	9	(1)	7
Zn	946	(44)	6	495	(8)	1	89	(12)	12	46	(3)	9	8	(1)	18
Ga	984	(98)	2	487	(45)	3	93	(4)	7	49	(4)	2	11	(0)	12
Ge	938	(136)	7	494	(48)	1	99	(10)	2	52	(3)	4	14	(1)	29
Sr	1092	(106)	8	522	(79)	4	109	(34)	8	50	(0)	1	—	—	
Mo	987	(40)	1	519	(33)	4	106	(15)	6	49	(10)	1	9	(9)	18
Ag	900	(96)	11	449	(62)	11	89	(10)	12	49	(7)	1	9	(1)	10
Cd	1029	(50)	3	546	(33)	9	93	(6)	8	55	(3)	9	8	(0)	20
In	957	(85)	4	525	(35)	5	110	(18)	9	50	(4)	1	12	—	14
Ba	1024	(48)	2	379	(116)	32	85		17	45	(7)	11	—	—	

[a] Original contents of fluid-inclusion analogue samples.
[b] value: mean values of PIXE analyses of fluid-inclusion analogue samples (Table 3); SD = corresponding standard deviations (1σ; $n = 3$); err. = relative difference between the mean concentration and the original content; — = not calculated.

lean toward the bottom by gravity. Thus, X-rays from a small amount of fluid behind the halite were absorbed by the halite. However, X-ray absorption by halite and hypersaline fluid (24 wt.% NaCl, density = 1.2) are very similar (Vanko et al., 2001), so that the effect on the quantification is estimated to be small.

The large isolated inclusion (Fig. 4a) deviates relatively from the negative crystal shape but it can be approximated as an ellipsoid of gyration (spheroid). When a deviation of the shape from the spheroid is small, the approximation of fluid-inclusion shapes as spheroids is sufficient. The quantification error for PIXE fluid-inclusion analyses is linearly correlated with the uncertainty on estimates of inclusion volume. Fluid inclusions in trails 1, 2, and 3 have typical negative crystal shapes. For various negative-crystal shapes (variations of Figs. 28, 29, 40, in Frondel, 1962), uncertainties on the volume estimates for ellipsoids are calculated at 0.9–15.4%. The uncertainties depend on the ratio of width to length of the inclusions. Almost all fluid inclusions of trails 1 and 2 have the ratio of 1 to 1.5, so the uncertainties on the volume estimates for ellipsoids are calculated at 0.9–3.6%. The quantification errors due to a 3.6% volume error are estimated at ±3% for Ca, Mn, Fe, Cu, Zn, Sr, Br, Rb, and Pb, respectively. Elemental concentrations in paired fluid inclusions N-1 and N-2 are identical within the total analytical error, except for Ca and Cu (Table 6), although these inclusions differed from a negative-crystal shape (Fig. 4c,d). Thus, the approximation as ellipsoids appears to be a fairly good approximation for the present analyses. The compositional differences for Ca and Cu can be attributed to a physical separation of halite and bubble in the inclusions, because inclusion N-1 included halite and no bubble, whereas inclusion N-2 included a bubble and no halite (Fig. 4c,d).

Based on these considerations, it is thought that uncertainties due to these three factors are not large for the present analyses, and the total analytical error including these uncertainties is probably comparable to the total analytical error listed in Table 5.

5.2. Fluid Inclusion Analysis by PIXE: Comparison with Other Methods

In previous PIXE studies, Ryan et al. (1995) calculated an accuracy of ±15% for concentrations at the wt.% level in single fluid inclusions. The total error for PIXE analysis of natural fluid inclusions was of the order of ±30% relative (Ryan, 1999). For SRXRF analyses, Mavrogenes et al. (1995) and Vanko et al. (2001) estimated errors of ±10–40% relative at the wt.% level, and Philippot et al. (1998) obtained an error better than ±20% relative for concentrations of 1000–5000 ppm. For LAM-ICP-MS analyses, McCandless et al. (1997) and Ulrich et al. (1999) reported errors of ±20–30% relative for concentrations of several tens of ppm.

For the present measurements, the total analytical errors of ±11–40% relative (e.g., ±11% for Br and ±40% for Ca) were achieved for 10–1000 ppm concentrations. These total analytical errors are strongly affected by the uncertainty in the microscopic determination of the inclusion depth. Vanko et al. (1993) reported an accuracy of ±1 μm for the microscopic determination of inclusion depths. Ménez et al. (1999) proposed a precise method for the determination of inclusion depths (at ±0.5 μm) by using nuclear reaction resonance between proton beam and Na in fluid inclusions. By using the method, the total analytical error can be reduced to ±7% relative for Ca, ±2% for Fe, and ±1% for Zn, Br, and Sr, for measurements of spherical fluid inclusions with 30 μm radius and 20 μm depth in quartz.

Detection limits for the analysis of single fluid inclusions by PIXE and SRXRF depend on measurement geometry, beam conditions, integrated charges, type of filter in front of the detector, inclusion depth, and element of interest; consequently, comparison is difficult. In the present study, we obtained a detection limit of ca. 5.7×10^{-13} g for transition metal elements, which is higher than the detection limit of ca. 7.9×10^{-14} g from previous PIXE measurements with different analytical conditions (Ryan et al., 1993). In a SRXRF study,

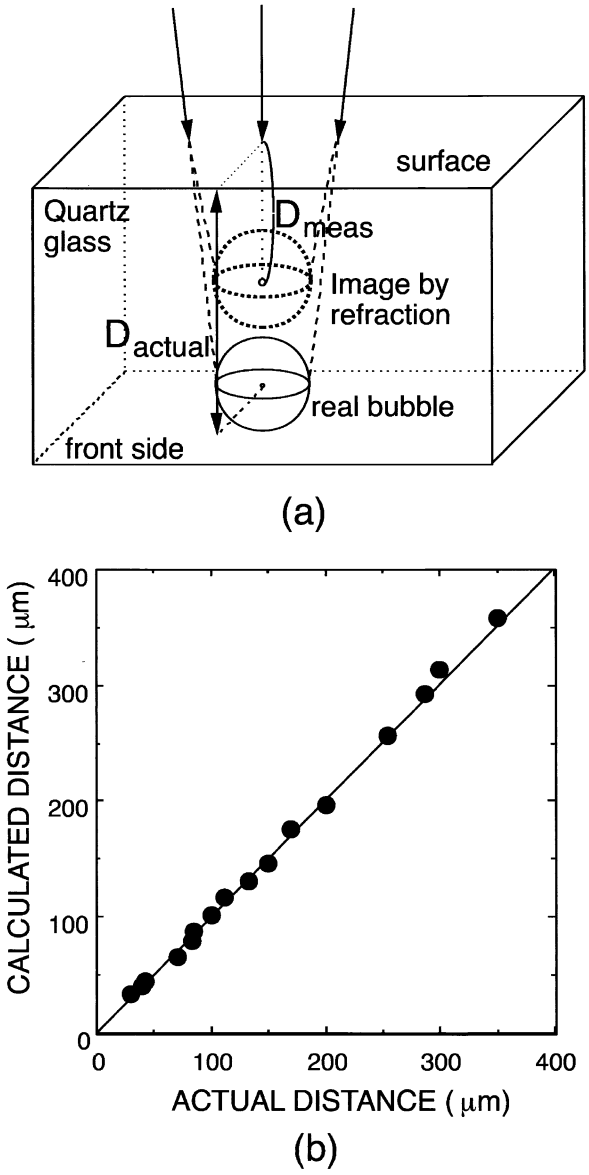

Fig. 7. (a) Schematic diagram illustrating the microscopic measurement of the distance between the waist of a bubble in a quartz glass and the glass surface. The distance measured from the surface by a microscope (D_{meas}) is affected by refraction by the matrix and by errors associated with the microscope (adjustment of the fine focus knob and aberration of the optics). Thus, by comparing the measured distance corrected for refraction and the actual distance (D_{actual}), the errors due to the microscope can be estimated. D_{actual} is easily determined by observation of the bubble from the front face because the bubble leans to the front and measurement can be made without the refraction. (b) Relationship between the distance calculated based on the measured distance (D_{meas}) and the actual distance (D_{actual}).

Vanko et al. (2001) statistically estimated a detection limit of 2.1×10^{-14} g for Cu (their empirical, estimated value was 1.6×10^{-13} g). Still lower detection limits could be realized with our PIXE instrument by improving the measurement conditions, for example through the application of different filters.

Table 5. Detection limits and errors due to depth uncertainty for PIXE quantification of trace elements in fluid inclusions.

	Atomic number	Detection limit[a] (ppm)	Error due to ±2.6 μm depth uncertainty[b] (rel. %)	Total analytical error[c] (rel. %)
Ca	20	5747	+28/−39	40
Cr	24	99	+12/−13	20
Mn	25	46	+10/−11	18
Fe	26	24	+9/−9	16
Ni	28	9	+6/−7	14
Cu	29	7	+6/−7	14
Zn	30	5	+5/−6	13
Ga	31	4	+5/−5	12
Ge	32	4	+5/−5	12
Br	35	4	+4/−4	11
Rb	37	4	+4/−4	11
Sr	38	5	+5/−5	12
Mo	42	8	+4/−4	11
Ag	47	20	+5/−5	12
Cd	48	24	+4/−4	11
In	49	31	+4/−4	11
Ba	56	291	+5/−5	12
Pb	82	14	+6/−6	13

[a] Detection limits for measurements of spherical fluid inclusions with a 30 μm radius and 20 μm depth. These limits were calculated from 3 times the statistical error for the computed backgrounds and the overlapping peak intensities at an integrated charge of 1.0 μC.

[b] Error due to depth uncertainty represents the effects on calculated results, if measured inclusion depths are 2.6 μm too deep or too shallow.

[c] Total analytical error is estimated from the sum total of the error for the PIXE measurements (±7%) and mean values of the error due to the depth uncertainty.

5.3. Chemical Features of Fluid Inclusions in Hydrothermal Quartz

Concentrations for each element in the natural fluid inclusions analyzed are comparable to those from other hydrothermal veins and ores related to granite (Ryan et al., 1991; Heinrich et al., 1992; Audétat et al., 2000a; Vanko et al., 2001).

High Ge contents were observed in fluid inclusions of trail 3 (Table 6). Although quartz from igneous rocks usually contains 0.8–3.3 ppm Ge (Bernstein, 1985), this element was not detected with PIXE in our quartz. In addition, Ge tends to be concentrated in late hydrothermal fluids as a result of the fractional crystallization of igneous fluids or due to incorporation of Ge from the country rocks (Bernstein, 1985). Ge contents of 70–500 ppm were reported from enargite in hydrothermal ore deposits near the quartz vein (Ando, 1964), indicating a transportation of Ge by hydrothermal fluids related to granite formation. Thus, the Ge observed is thought to be present in the fluid inclusions. Small X-ray peaks of Ba, La, and Ce were also visible in the large isolated fluid inclusions (Fig. 8a). Several tens to hundreds of ppm Ba, La, and Ce were observed in some hypersaline fluid inclusions related to granite (Audétat et al., 2000a, b).

In trail 1, a large variation of Cu contents, of two orders of magnitude, was observed (Fig. 9). Although the effect of Cu from the matrix has been corrected for, an overestimation of Cu

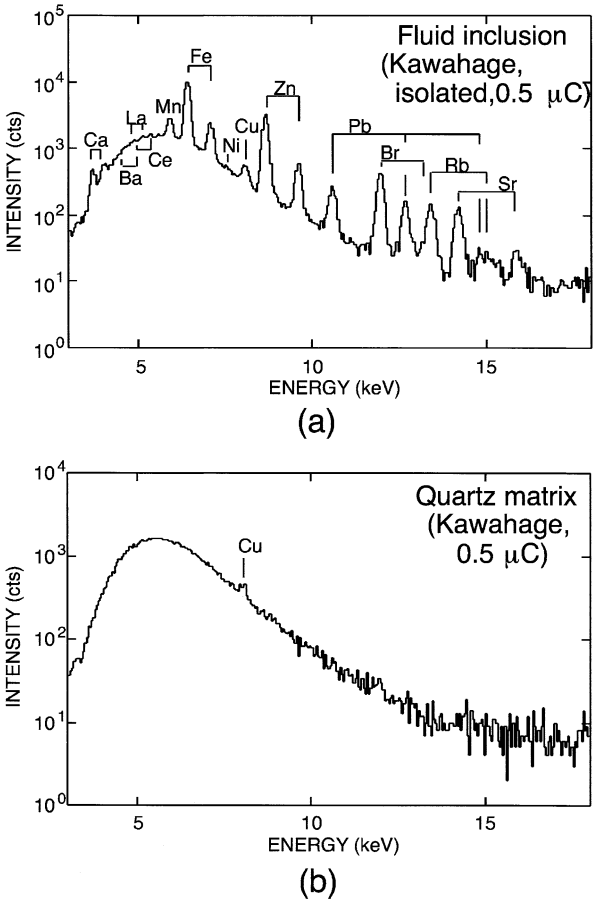

Fig. 8. (a) X-ray spectrum of a large isolated fluid inclusion (sample O) in a quartz crystal from Kawahage. (b) X-ray spectrum of the quartz matrix. The spectra were measured by PIXE (4-MeV protons, 1.3-mm-thick graphite filter, integrated charge of 0.5 μC).

contents in fluid inclusions may occur when submicrometer solid inclusions bearing Cu are present in the quartz, and are distributed heterogeneously in the quartz matrix. To understand the cause of the large Cu variation, future work is required.

Elemental concentrations in fluid inclusions of trail 1 are positively correlated with each other, except for Cu and Rb (Fig. 10). The correlation for trail 2 data is also shown in Figure 10. This result demonstrates that elemental ratios in fluid inclusions of trails 1 and 2 are basically unchanged over a range of elemental concentrations. The trend may be explained by enrichment of solutes due to water loss from the inclusions during secondary migration of the inclusions from the original fracture plane and/or formation of negative-crystal shapes (Audétat and Günther, 1999). Assuming water loss from inclusions, relative degrees of water loss of 30–80% can be estimated for the inclusions of trail 1. The apparent NaCl salinity of these inclusions is fairly constant (Table 2). Thus, the observed elemental correlation could be due to other mechanisms. Detailed fluid inclusion studies using a coupling of PIXE and microthermometry are important to elucidate the process. Elemental ratios of fluid inclusions remained basically unchanged by the process, so that such ratios provide important information for elucidating the original chemistry of a hydrothermal fluid.

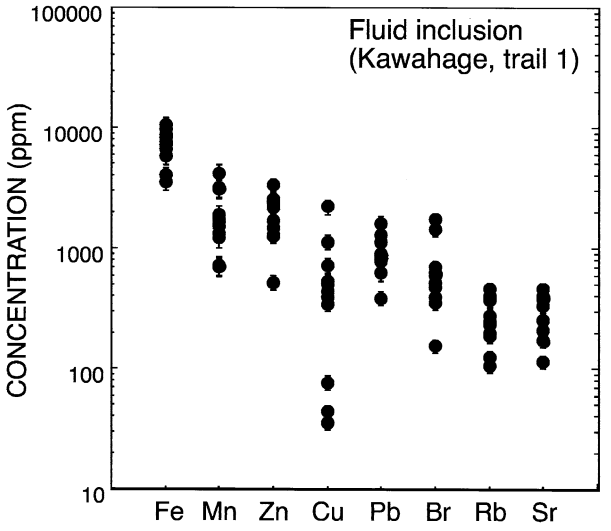

Fig. 9. Elemental concentrations in 11 secondary fluid inclusions of trail 1 in a quartz crystal from Kawahage. The error bars represent the total analytical errors (Table 5).

6. CONCLUSION

We have shown that the PIXE method is capable of determining elements at the ppm level in a single fluid inclusion with a relative mean error of ±7%. For natural inclusions in quartz, we estimated a total analytical error of ±40% relative for Ca, ±16% for Fe, ±13% for Zn, ±12% for Sr, and ±11% for Rb and Br, which includes uncertainty at microscopic

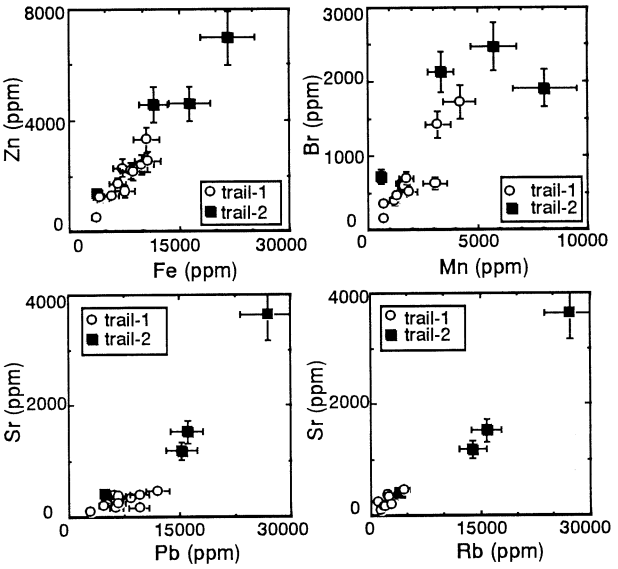

Fig. 10. Relationship between concentrations of Zn and Fe, Br and Mn, Sr and Pb, and Sr and Rb in secondary fluid inclusions on trails 1 and 2 in a quartz crystal from Kawahage. The error bars represent the total analytical errors (Table 5).

Table 6. PIXE analyses for single fluid inclusions in a quartz crystal from the Kawahage quartz vein.

	G-1 (trail 1)		G-2 (trail 1)		G-3 (trail 1)		G′-1 (trail 1)		G′-2 (trail 1)		F-4 (trail 1)		F-3 (trail 1)		F-2 (trail 1)		F-1 (trail 1)		H-1 (trail 1)		H-2 (trail 1)		J-1 (trail 2)	
	Conc. (ppm)	Int. (cts)	Conc. (ppm)	Int. (cts)	Conc. (ppm)	Int. (cts)	Conc. (ppm)	Int. (cts)	Conc. (ppm)	Int. (cts)	Conc. (ppm)	Int. (cts)	Conc. (ppm)	Int. (cts)	Conc. (ppm)	Int. (cts)	Conc. (ppm)	Int. (cts)	Conc. (ppm)	Int. (cts)	Conc. (ppm)	Int. (cts)	Conc. (ppm)	Int. (cts)
Ca	—	—	—	—	—	—	—	—	—	—	—	—	—	—	—	—	—	—	—	—	—	—	78807	(185)
Mn	1208	(1796)	726	(1220)	1310	(1520)	3191	(1613)	705	(62)	1520	(1862)	3063	(2101)	1878	(1749)	1635	(1850)	4183	(1119)	1745	(1005)	3319	(2223)
Fe	4047	(7340)	3534	(7310)	5781	(8120)	10536	(6374)	7511	(834)	7137	(10065)	9789	(7808)	8310	(8934)	6593	(8597)	10642	(3390)	8644	(6054)	11493	(9875)
Cu	76	(412)	36	(341)	44	(327)	445	(388)	2193	(398)	509	(898)	729	(779)	344	(560)	390	(693)	1131	(444)	529	(473)	206	(326)
Zn	1257	(2378)	520	(1158)	1291	(1851)	3299	(1734)	1456	(169)	2295	(2831)	2399	(1723)	2201	(2082)	1700	(1942)	2525	(687)	2153	(1390)	4548	(4322)
Ge	—	—	—	—	—	—	—	—	—	—	—	—	—	—	—	—	—	—	—	—	—	—	—	—
Br	398	(309)	154	(142)	474	(277)	1419	(241)	351	(14)	628	(302)	629	(178)	516	(191)	594	(265)	1728	(151)	700	(149)	2133	(704)
Rb	187	(101)	123	(79)	197	(80)	464	(49)	397	(10)	400	(131)	377	(73)	234	(59)	105	(32)	277	(15)	248	(33)	1588	(333)
Sr	174	(76)	114	(59)	174	(57)	461	(38)	406	(8)	403	(107)	389	(61)	381	(78)	256	(63)	212	(9)	337	(35)	1536	(252)
Pb	845	(344)	388	(188)	1266	(388)	1600	(145)	1279	(27)	823	(207)	886	(131)	786	(152)	892	(208)	621	(29)	1121	(127)	2131	(374)

	J-2 (trail 2)		J-3 (trail 2)		J-4 (trail 2)		K-1 (trail 3)		K-2 (trail 3)		K-3 (trail 3)		K-4 (trail 3)		M-1 (isolated)		O-1 (isolated)		N-1 (necking)		N-2 (necking)	
	Conc. (ppm)	Int. (cts)	Conc. (ppm)	Int. (cts)	Conc. (ppm)	Int. (cts)	Conc. (ppm)	Int. (cts)	Conc. (ppm)	Int. (cts)	Conc. (ppm)	Int. (cts)	Conc. (ppm)	Int. (cts)	Conc. (ppm)	Int. (cts)	Conc. (ppm)	Int. (cts)	Conc. (ppm)	Int. (cts)	Conc. (ppm)	Int. (cts)
Ca	61977	(575)	—	—	18872	(261)	—	—	—	—	—	—	—	—	1855	(180)	6781	(1018)	23762	(914)	94094	(330)
Mn	8039	(4646)	5745	(331)	610	(903)	—	—	—	—	—	—	—	—	555	(4429)	365	(4553)	929	(1893)	1270	(1103)
Fe	16450	(11474)	21624	(1819)	3741	(6796)	—	—	—	—	—	—	—	—	1535	(14783)	2198	(33103)	3329	(8128)	2753	(3051)
Cu	582	(535)	2911	(504)	168	(440)	184	(729)	271	(627)	162	(603)	574	(674)	60	(690)	71	(1275)	741	(2047)	1280	(1886)
Zn	4584	(2863)	6961	(909)	1375	(2398)	—	—	—	—	—	—	—	—	293	(2613)	891	(12466)	819	(1757)	859	(1034)
Ge	—	—	—	—	—	—	65	(133)	72	(83)	29	(56)	44	(26)	—	—	—	—	—	—	—	—
Br	1907	(389)	2466	(121)	729	(423)	—	—	—	—	—	—	—	—	136	(396)	400	(1834)	434	(302)	420	(175)
Rb	1401	(178)	2725	(88)	402	(146)	—	—	—	—	—	—	—	—	42	(77)	214	(612)	201	(87)	239	(63)
Sr	1187	(118)	3647	(92)	429	(122)	—	—	—	—	—	—	—	—	64	(91)	246	(550)	145	(49)	174	(36)
Pb	2034	(221)	3593	(97)	651	(201)	109	(58)	88	(26)	76	(39)	310	(47)	77	(120)	491	(1202)	156	(58)	163	(36)

Conc. = concentration; Int. (cts) = measured X-ray intensity (counts). — = undetected.

measurements of inclusion depths. Uncertainties due to the presence of hypersaline fluid, halite daughter crystals, and deviation from spheroidal inclusion shape are smaller than the total analytical error. Thus, the effect for the present inclusion analyses is probably small. At an integrated charge of 1.0 μC, we achieved detection limits of 4 to 46 ppm for elements of mass numbers 25–50 for spherical fluid inclusions with 30 μm radius and 20 μm depth in quartz.

In the PIXE analysis of natural fluid inclusions in a hydrothermal quartz crystal, the elemental concentrations in the inclusions varied widely. The large compositional variation arises basically from trapping of various fluids in the single quartz crystal. In trails of fluid inclusions formed from a specific fluidization event, we observed an order of magnitude variation in element concentrations. Further fluid inclusion studies, coupled with PIXE analysis and microthermometry, are required to understand the causes of this effect.

Acknowledgments—We are grateful to the late Prof. Shigeho Sueno (University of Tsukuba) for construction of the PIXE facility and the late Mr. Teruo Shingu (Crestec Co. Ltd.) for construction of a routine PIXE analytical system. We also wish to thank A. Audétat, P. Philippot, and an anonymous reviewer for their constructive reviews.

Associate editor: U. Reimold

REFERENCES

Ando A. (1964) *Geochemistry of germanium in the metallic sulfide ore deposits in Japan*. Rep. Geol. Surv. Japan **208,** 72 p. (in Japanese with English abstract).

Audétat A. and Günther D. (1999) Mobility and H_2O loss from fluid inclusions in natural quartz crystal. *Contrib. Mineral. Petrol.* **137,** 1–14.

Audétat A., Günther D., and Heinrich C. A. (1998) Formation of a magmatic-hydrothermal ore deposit: Insights with LA-ICP-MS analysis of fluid inclusions. *Science* **279,** 2091–2094.

Audétat A., Günther D., and Heinrich C. A. (2000a) Causes for large-scale metal zonation around mineralized plutons: Fluid inclusion LA-ICP-MS evidence from the Mole granite, Australia. *Econ. Geol.* **95,** 1563–1581.

Audétat A., Günther D., and Heinrich C. A. (2000b) Magmatic hydrothermal evolution in a fractionating granite: A microchemical study of the Sn-W-F-mineralized Mole granite. *Geochim. Cosmochim. Acta* **64,** 3373–3393.

Ballhaus C., Ryan C. G., Mernagh T. P., and Green D. H. (1994) The partitioning of Fe, Ni, Cu, Pt, and Au between sulfide, metal, and fluid phases: A pilot study. *Geochim. Cosmochim. Acta* **58,** 811–826.

Berger M. J., Hubbell J. H. (1987) NBSIR 87–3597. National Institute of Standards and Technology, Gaithersburg, MD.

Bernstein L. R. (1985) Germanium geochemistry and mineralogy. *Geochim. Cosmochim. Acta* **49,** 2409–2422.

Campbell J. L. (1995) Instrumentation, fundamentals, and quantification. In *Particle-Induced X-ray Emission Spectrometry (PIXE)* (eds. S. A. E. Johansson, J. L. Campbell, and K. G. Malmqvist), pp. 19–100. John Wiley, New York.

Cohen D. D. and Harrigan M. (1985) K- and L-shell ionization cross sections for protons and helium ions calculated in the ECPSSR theory. *At. Data Nucl. Data Tables.* **33,** 255–343.

Czamanske G. K., Sisson T. W., Campbell J. L., and Teesdale W. J. (1993) Micro-PIXE analysis of silicate reference standards. *Am. Mineral.* **78,** 893–903.

Damman A. H., Kars S. M., Touret J. L. R., Rieffe E. C., Kramer J. A. L. M., Vis R. D., and Pintea I. (1996) PIXE and SEM analyses of fluid inclusions in quartz crystals from the K-alteration zone of the Rosia Poieni porphyry-Cu deposit, Apuseni Mountains, Rumania. *Eur. J. Mineral.* **8,** 1081–1096.

Frantz J. D., Mao H. K., Zhang Y.-G., Wu Y., Thompson A. C., Underwood J. H., Giauque R. D., Jones K. W., and Rivers M. L. (1988) Analysis of fluid inclusions by X-ray fluorescence using synchrotron radiation. *Chem. Geol.* **69,** 235–244.

Frondel C. (1962) Quartz. In *The System of Mineralogy*, 7th ed., *Vol. III, Silica Minerals*, pp. 9–250. John Wiley, New York.

Götze J., Tichomirowa M., Fuchs H., Pilot J., and Sharp Z. D. (2001) Geochemistry of agates: A trace element and stable isotope study. *Chem. Geol.* **175,** 523–541.

Günther D., Audétat A., Frischknecht R., and Heinrich C. A. (1998) Quantitative analysis of major, minor and trace elements in fluid inclusions using laser ablation inductively coupled plasma mass spectrometry. *J. Anal. Atom. Spectrom.* **13,** 263–270.

Heinrich C. A., Ryan C. G., Mernagh T. P., and Eadington P. J. (1992) Segregation of ore metals between magmatic brine and vapor: A fluid inclusion study using PIXE microanalysis. *Econ. Geol.* **87,** 1566–1583.

Horn I., Hinton R. W., Jackson S. E., and Longerich H. P. (1997) Ultra-trace element analysis of NIST SRM 616 and 614 using laser-ablation microprobe- inductively coupled plasma- mass spectrometry (LAM-ICP-MS): A comparison with secondary ion mass spectrometry (SIMS). *Geostand. Newsl.* **21,** 191–203.

International Commission on Radiation Units and Measurements (1993) Stopping powers and ranges for protons and alpha particles. *ICRU Rep.* **49,** 117–180.

Jackson S. E., Longerich H. P., Dunning G. R., and Fryer B. J. (1992) The application of laser-ablation microprobe-inductively coupled plasma-mass spectrometry (LAM-ICP-MS) to in situ trace element determinations in minerals. *Can. Mineral.* **30,** 1049–1064.

Kurosawa M., Sueno S., Shima K., Ohshima H., Ishii S., Kamiya H., Kimoto S., Ohyi H., and Hayashi K. (1998) Development of a new sample chamber for proton microprobe analysis of mineral samples. *Nucl. Instrum. Methods Phys. Res.* **B142,** 599–605.

Kurosawa M., Campbell J. L., Teesdale W. J., Ohyi H., Deguchi Y., and Murao S. (1999) Quantitative trace element analyses of silicate reference materials and a stainless steel using the proton microprobe. *Chem. Geol.* **160,** 241–250.

Mavrogenes J. A., Bodnar R. J., Anderson A. J., Bajt S., Sutton S. R., and Rivers M. L. (1995) Assessment of the uncertainties and limitations of quantitative elemental analysis of individual fluid inclusions using synchrotron X-ray fluorescence (SXRF). *Geochim. Cosmochim. Acta* **59,** 3987–3995.

Maxwell J. A., Campbell J. L., and Teesdale W. J. (1989) The Guelph PIXE software package. *Nucl. Instrum. Methods Phys. Res.* **B43,** 218–230.

Maxwell J. A., Teesdale W. J., and Campbell J. L. (1995) The Guelph PIXE software package II. *Nucl. Instrum. Methods Phys. Res.* **B95,** 407–421.

McCandless T. E., Lajack D. J., Ruiz J., and Ghazi A. M. (1997) Trace element determination of single fluid inclusions in quartz by laser ablation ICP-MS. *Geostand. Newsl.* **21,** 279–287.

Ménez B., Philippot P., Bonnin-Mosbah M., and Gibert F. (1999) Fluid inclusion depth and thickness estimates using Na nuclear reaction resonance and Si elastic scattering. *Nucl. Instrum. Methods Phys. Res.* **B158,** 533–537.

Ménez B., Philippot P., Bonnin-Mosbah M., Simionovici A., and Gibert F. (2002) Analysis of individual fluid inclusions using Synchrotron X-ray Fluorescence microprobe: Progress toward calibration for trace element. *Geochim. Cosmochim. Acta* **66,** 561–576.

Mosbah M., Clocchiatti R., Michaud V., Piccot D., Chevallier P., Legrand F., Als Nilsen G., and Grübel G. (1995) Micro PIXE and micro SXRF: Comparison of the two methods and application to glass inclusions from volcano (Eolian Islands-Italy). *Nucl. Instrum. Methods Phys. Res.* **B104,** 481–488.

Paul H. and Sacher J. (1989) Fitted empirical reference cross sections for K-shell ionization by proton. *At. Data Nucl. Data Tables* **42,** 105–156.

Philippot P., Ménez B., Chevallier P., Gibert F., Legrand F., and Populus P. (1998) Absorption correction procedures for quantitative analysis of fluid inclusions using synchrotron radiation X-ray fluorescence. *Chem. Geol.* **144,** 121–136.

Philippot P., Ménez B., Drakopoulos M., Simionovici A., Snigirev A., and Snigireva I. (2001) Mapping trace-metal (Cu, Zn, As) distribution in a single fluid inclusion using a third generation synchrotron light source. *Chem. Geol.* **173,** 151–158.

Rankin A. H., Ramsey M. H., Coles B., Van Langevelde F., and Thomas C. R. (1992) The composition of hypersaline, iron-rich granitic fluids based on laser-ICP and synchrotron-XRF microprobe analysis of individual fluid inclusions in topaz, Mole granite, eastern Australia. *Geochim. Cosmochim. Acta* **56,** 67–79.

Reuter W., Lurio A., Cardone F., and Ziegler J. F. (1975) Quantitative analysis of complex targets by proton-induced x rays. *J. Appl. Phys.* **46,** 3194–3202.

Ryan C. G. (1999) Advances in fluid inclusion analysis using the nuclear microprobe. *Nucl. Instrum. Methods Phys. Res.* **B158,** 523–532.

Ryan C. G., Cousens D. R., Sie S. H., Griffin W. L., and Suter G. F. (1990) Quantitative PIXE microanalysis of geological material using the CSIRO proton microprobe. *Nucl. Instrum. Methods Phys. Res.* **B47,** 55–71.

Ryan C. G., Cousens D. R., Heinrich C. A., Griffin W. L., Sie S. H., and Mernagh T. P. (1991) Quantitative PIXE microanalysis of fluid inclusions based on a layered yield model. *Nucl. Instrum. Methods Phys. Res.* **B54,** 292–297.

Ryan C. G., Heinrich C. A., and Mernagh T. P. (1993) PIXE microanalysis of fluid inclusions and its application to study ore metal segregation between magmatic brine and vapor. *Nucl. Instrum. Meth. Phys. Res.* **B77,** 463–471.

Ryan C. G., Heinrich C. A., van Achterbergh E., Ballhaus C., and Mernagh T. P. (1995) Microanalysis of ore-forming fluids using the scanning proton microprobe. *Nucl. Instrum. Methods Phys. Res.* **B104,** 182–190.

Shepherd T. J. and Chenery S. R. (1995) Laser ablation ICP-MS elemental analysis of individual fluid inclusions: An evaluation study. *Geochim. Cosmochim. Acta* **59,** 3997–4007.

Sterner S. M., Hall D. L., and Bodnar R. J. (1988) Synthetic fluid inclusions. V. Solubility relations in the system NaCl-KCl-H_2O under vapor-saturated conditions. *Geochim. Cosmochim. Acta* **52,** 989–1005.

Ulrich T., Günther D., and Heinrich C. A. (1999) Gold concentrations of magmatic brines and the metal budget of porphyry copper deposits. *Nature* **399,** 676–679.

Vanko D. A., Sutton S. R., Rivers M. L., and Bodnar R. J. (1993) Major-element ratios in synthetic fluid inclusions by synchrotron X-ray fluorescence microprobe. *Chem. Geol.* **109,** 125–134.

Vanko D. A., Bonnin-Mosbah M., Philippot P., Roedder E., and Sutton S. R. (2001) Fluid inclusion in quartz from oceanic hydrothermal specimens and the Bingham, Utah porphyry-Cu deposit: A study with PIXE and SXRFM. *Chem. Geol.* **173,** 227–238.

Weil J. A. (1984) A review of electron spin spectroscopy and its application to the study of paramagnetic defects in crystalline quartz. *Phys. Chem. Minerals* **10,** 149–165.

Weise G., Schrön W., and Uschmann W. (1993) Spurenelementgehalte in Bergkristtallen ("Tiefengrubener Diamanten") bei Bad Berka (Thüringen). *N. Jb. Miner. Mh.* **1993,** 363–373.

APPENDIX 1

PIXE QUANTIFICATION

In the general quantification of PIXE results, the intensities of generated X-rays can be obtained from first principles by using a database of physical quantities such as stopping powers, ionization cross sections, and attenuation coefficients (Reuter et al., 1975). For a sample of a given thickness, the measured X-ray intensity, Y_i, of the K line of element i detected is described as follows (Campbell, 1995):

$$Yi = \frac{Si}{\sigma i,\,4MeV}\,Ci\rho B\iiint \sigma i(x,y,z)Ti(x,y,z)dxdydz \qquad (A1)$$

$$S_i = \frac{N_{av}\omega_i r_i \tau_i \varepsilon_i(\Omega/4\pi)}{A_i}\sigma_i,4MeV \qquad (A2)$$

S_i is the sensitivity factor of element i and is defined as the X-ray yield per proton per unit concentration per unit areal density. C_i is the concentration of element i, ρ is the specimen's density (g cm^{-3}), and B is the integrated charge of protons over the irradiated area (μC cm^{-2}). $\sigma_i(x,y,z)$ is the K X-ray production cross section (cm^2) at the degraded proton energy at a discrete point (x,y,z) in the sample, and $T_i(x,y,z)$ is the absorption of the K X-ray of element i originating at coordinate (x,y,z) due to the path length through the sample material. N_{av} is Avogadro's number, ω_i is the K-shell fluorescence yield of the incident proton energy, r_i is the line intensity fraction, τ_i is the transmission through the filter interposed between the specimen and the detector, ε_i is the detector's intrinsic efficiency, $(\Omega/4\pi)$ is the fractional solid angle subtended by the detector, and A_i is the atomic mass of element i (g). The measured X-ray intensity, Y_i, of the L line of element i can be defined similarly.

The X-ray intensities (area intensities) are determined by fitting gaussian peaks onto each elemental peak and by subtracting the continuum background. For peak overlapping from two elements, intensity for an element of interest was calculated based on other K_α and K_β peak intensities measured for each element and the previous measured K_α/K_β area intensity ratio for each element at 4 MeV proton irradiation. X-ray spectra of vacant bubbles in quartz glasses, and extremely vapor-rich (leaked out?) fluid inclusions are almost identical to spectra of the quartz glass matrix and the quartz matrix, respectively. Thus, the background subtraction for the analog and the natural samples was based on assuming a linear background for low- and high-energy tails of interest peaks, taking into account the shapes of spectra for glass matrix and quartz matrix. Statistical errors for peak fitting plus background subtraction depend on area intensities and are estimated at $\pm$0.3–1% relative for the intensities of ten thousands of counts, $\pm$1–5% for thousands of counts, $\pm$5–10% for hundreds of counts, and $\pm$10–20% for several tens of counts, respectively.

The sensitivity factor S_i is determined by measurements of thin-film standards for 1 μC of 4-MeV protons (Appendix 2), so S_i in Eqn. A1 is normalized by the K X-ray production cross section at 4 MeV ($\sigma_{i,4MeV}$). In Eqn. A1, $\sigma_i(x,y,z)$ is calculated from proton energy at coordinate (x,y,z), $E_{p,z}$, and the K shell and L shell ionization cross sections for each energy (Paul and Sacher, 1989; Cohen and Harrigan, 1985). $E_{p,z}$ (MeV) was calculated by integration of the energy loss (stopping power) in the sample materials (ICRU, 1993) and by determining the beam path up to the coordinate (x,y,z). $T_i(x,y,z)$ was calculated based on the mass attenuation coefficient of the materials for X-rays of element i and the path lengths of X-rays through the materials. The mass attenuation coefficient was calculated using NIST XCOM data (Berger and Hubbell, 1987).

For fluid inclusion analyses, $\sigma_i(x,y,z)$ and $T_i(x,y,z)$ are required to integrate over the inclusion volume, taking into account the difference of matrix (SiO_2) and fluid (H_2O). The present quantification was performed based on the model by Ryan et al. (1993). The geometry for the calculations is shown in Figure 2. Since natural fluid inclusions often have a negative-crystal shape, an ellipsoidal shape was assumed. The ellipsoidal, homogeneous fluid inclusion (half-length *l*, half-width *w*, and half-thickness *t*) is buried in a homogeneous matrix. The incident beam angle is normal to the sample surface with an X-ray take-off angle of 45°. The Z-axis is defined as the direction of the incident beam, and the X- and Y-axes are normal to the Z-axis.

For calculations of $\sigma_i(x,y,z)$, the proton energy, $E_{p,z,f\text{-}i}$, at coordinate (x,y,z) in the inclusion is required. $E_{p,z,f\text{-}i}$ is expressed using Eqns. A3–A5; the path lengths of incident protons through the matrix, Mp, and the fluid, Fp, are as follows:

$$E_{p,z,f-i} = 1.6875\sqrt{1.747/1.590\sqrt{4^{1.590} - 1.590 \times 183.0 \cdot \rho_{SiO_2} \cdot M_p - 1.747 \times 248 \cdot \rho_{H_2O} \cdot F_p}} \qquad (A3)$$

$$F_p = \left| z - \sqrt{t^2 \cdot \left(1 - \frac{x^2}{l^2} - \frac{y^2}{w^2}\right)} \right| \quad \text{(A4)}$$

$$M_p = \left| t + d - \sqrt{t^2 \cdot \left(1 - \frac{x^2}{l^2} - \frac{y^2}{w^2}\right)} \right| \quad \text{(A5)}$$

ρ_{SiO2} and ρ_{H_2O} are the densities of SiO_2 and water, respectively.

In addition, $T_{i,f\text{-}i}(x,y,z)$ is described by using the path lengths of the X-rays through the matrix, Mx, and the fluid, Fx, respectively, as follows:

$$T_{i,f-i} = \exp\left\{ -\left(\frac{\mu}{\rho}\right)_{i,SiO_2} \cdot \rho_{SiO_2} \cdot M_x - \left(\frac{\mu}{\rho}\right)_{i,H_2O} \cdot \rho_{H_2O} \cdot F_x \right\} \quad \text{(A6)}$$

$$F_x = \sqrt{2} \cdot \left| \frac{t^2 wx + l^2 wz + lt \cdot \sqrt{-w^2(x-z)^2 + l^2(w^2 - y^2) + t^2(w^2 - y^2)}}{(l^2 + t^2)w} \right| \quad \text{(A7)}$$

$$M_x = \sqrt{2} \cdot \left| \frac{l^2 wx(t+d) + t^2 w(t+d-x-z) - lt \cdot \sqrt{-w^2(x-z)^2 + l^2(w^2 - y^2) + t^2(w^2 - y^2)}}{(l^2 + t^2)w} \right| \quad \text{(A8)}$$

To simplify the numerical integration of Eqns. A3 and A6, the coordinates (x,y,z) were converted to polar coordinates as follows:

$$\begin{pmatrix} x \\ y \\ z \end{pmatrix} = \begin{pmatrix} r\, l \sin\theta\cos\phi \\ r\, w \sin\theta\sin\phi \\ r\, t \cos\theta \end{pmatrix} \quad \text{(A9)}$$

r is the distance between the origin and the coordinate (x,y,z), θ is the angle between r and the X-axis, and ϕ is the angle between the distance r and the Y-axis. By coordinate transformation, the triple integral in Eqn. A1 can be rewritten as follows:

$$Fi = \int\int\int f(k) r^2 \, dr d\theta d\phi \quad \text{(A10)}$$

$$f(k) = l\, w\, t\, r^2 \sin\theta \exp\left\{ \sum_{n=0}^{5} C_n \ln(E_{p,z,f-i})^n - \left(\frac{\mu}{\rho}\right)_{i,SiO_2} \cdot \rho_{SiO_2} \cdot M_x - \left(\frac{\mu}{\rho}\right)_{i,H_2O} \cdot \rho_{H_2O} \cdot F_x \right\} \quad \text{(A11)}$$

Equation 10 was numerically integrated using the 10-point Gauss-Legendre rule with intervals $0 \le r \le 1$, $0 \le \theta \le 1$, and $0 \le \phi \le 2\pi$.

Because natural fluid inclusions include bubbles, a correction needs to be applied in calculating F_i. X-ray intensities from a fluid inclusion including a bubble are represented as subtraction of X-ray intensities from two volumes (Ryan et al., 1993): the fluid inclusion volume that is fluid (no bubbles) and a volume of fluid corresponding to the bubble volume. In the present calculation, a correction for the bubble was performed based on the model of Ryan et al. (1993). For fluid inclusion analog samples, a fraction of the inclusions (bubbles) truncated by a quartz glass surface was also corrected for by subtracting the truncation volume from the sphere volume. In addition, a correction is required for X-ray intensities generated from trace impurities in the matrix. This correction was carried out by calculations for subtraction of two intensities: X-rays generated from the matrix of a cylindrical volume corresponding to the beam pass; and X-rays generated from the SiO_2 matrix corresponding to the inclusion volume.

APPENDIX 2

DETERMINATION OF THE SENSITIVITY CURVE OF THE DETECTOR

Before inclusion analyses, a thin-film multielement reference sample was used to determine the detector sensitivity (X-ray yield per proton per unit concentration per unit areal density) for each element. The thin-film sample was prepared by dropping 0.2 μL of an XTC-535 standard solution onto a 3-μm-thick Mylar film and drying the film in a desiccator. XSTC-535 (SPEX Co. Ltd., Metuchen, New Jersey) solution contained 1000 ppm each of Cr, Ni, Fe, Zn, Ga, Ge, Sr, Mo, Ag, Cd, In, and Ba in a 5% nitric acid solution. The film was then mounted on a 3-mm-thick graphite plate and covered with a 10-μm-thick fused-quartz cover glass; the cover glass was fixed with a resin to prevent loss of volatile elements during beam irradiation in the vacuum chamber. In measurements of thin-film samples without cover glass, we observed loss of intensities for volatile elements such as Ga, Cd, and In. Thus, a sealed thin-film sample or solid reference material was preferred for determinations of the sensitivities. No impurities with concentrations of more than 1 ppm were detected in the cover glass by LAM-ICP-MS. The measured sensitivities were corrected for effects of energy loss of the incident beam and X-ray absorption by the cover glass.

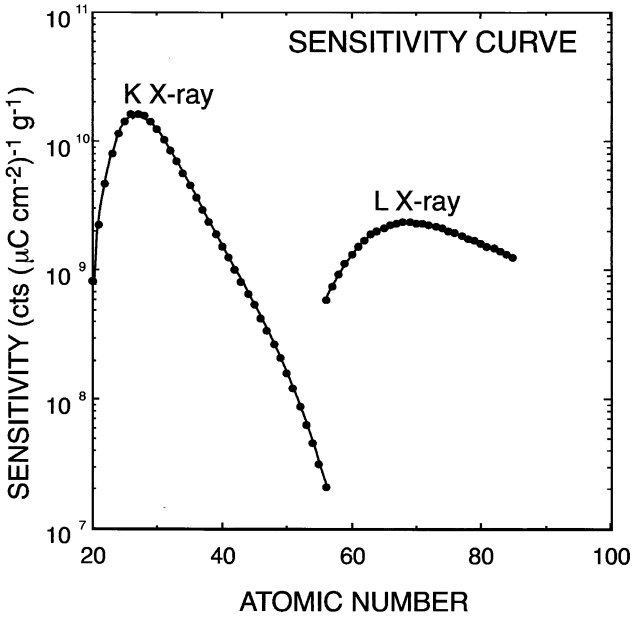

Fig. A1. Detector sensitivities for K and L X-rays (PIXE, 4-MeV protons, 1.3-mm-thick graphite filter). The sensitivities were calculated and determined from measurements on a thin-film multielement reference sample.

In addition, a multielement reference glass material, NIST SRM 1412, was used to determine detector sensitivity to the L X-rays of Pb and Ba. NIST SRM 1412 is an SiO_2-Al_2O_3 glass containing 4.55 wt.% each of Li_2O, B_2O_3, Na_2O, CaO, MgO, K_2O, ZnO, SrO, CdO, BaO, and PbO, and 0.03 wt.% FeO. The measured density of the NIST SRM 1412 was 2.85 g/cm^3. The measured sensitivities were corrected for effects of energy loss of the incident beam and X-ray absorption by matrix. A $5 \times 5 \times 2$ mm piece of the reference glass was mounted on a slide glass with resin. The NIST SRM 1412 sample and the thin-film sample were coated with a carbon film to prevent electrostatic charging and to measure the integrated charges.

These reference samples were analyzed by PIXE under the same conditions as those used for the fluid inclusion samples. The sensitivity curves determined for the K and L X-rays are shown in Fig. A1.